Journal of Volcanology and Geothermal Research 277 (2014) 22–35

Contents lists available at ScienceDirect

Journal of Volcanology and Geothermal Research

journal homepage: www.elsevier.com/locate/jvolgeores

Multi-scale reasonable attenuation tomography analysis (MuRAT): An imaging algorithm designed for volcanic regions

L. De Siena [a,*], C. Thomas [a], R. Aster [b,c]

[a] University of Münster, Institut für Geophysik, Correnstrasse 24, 48149 Münster, Germany
[b] Department of Earth and Environmental Science, New Mexico Tech, Socorro, NM, USA
[c] Geosciences Department, Warner College of Natural Resources, Colorado State University, Fort Collins, CO, USA

ARTICLE INFO

Article history:
Received 10 August 2013
Accepted 26 March 2014
Available online 8 April 2014

Keywords:
Attenuation tomography
Multi-step code
Scattering
Volcano imaging

ABSTRACT

The attenuation of body-wave amplitudes with propagation distance can be used to provide detailed tomographic images of seismic interfaces, fluid reservoirs, and melt batches in the crust. The high sensitivity of body-wave energies to high-scattering structures becomes an obstacle when we try to apply attenuation tomography to small-scale volcanic media, where we must take into account the complexities induced by strong heterogeneous scattering, topography, and uncertain source modeling in the recorded wave-fields. The MuRAT code uses a source- and site-independent coda-normalization method to obtain frequency-dependent measurements of *P*-to-coda and *S*-to-coda energy ratios. The code inverts these data for both the geometrical spreading factor and the spatially-dependent quality factors (Q), providing additional attenuation information in the regions where velocity tomography is available. The high sensitivity of coda-waves to highly heterogeneous structures highlights zones of anomalous scattering, which may corrupt amplitude-dependent attenuation measurements, and where basal assumptions of linear optics may go unfulfilled. A multi-step tomographic inversion increases the stability of the results obtained in regions of high heterogeneity (e.g., the volcanic edifice) by the inclusion of data corresponding to either sources or stations located in regions of lower heterogeneity. On the other hand, a mere increase in the number of rays entirely contained in the heterogeneous structures affects both the stability and the effective resolution of the results. We apply the code to two small waveform datasets recorded at an active (Mount St. Helens) and at a quiescent (Mount Vesuvius) volcano. The results show that the seismicity located inside or under the volcanic edifice produces an increase of the low-frequency energy ratios with travel time in both areas. In our interpretation, the anomalous concentration of energy which affects any waveform recorded on the cone, produced inside the volcanic edifice or in the feeding system of the volcano is due to seismic source- or medium-dependent resonance. The results also provide spatial and frequency limits on the feasibility of attenuation tomography in these two regions with larger datasets.

© 2014 Elsevier B.V. All rights reserved.

1. Introduction

Passive seismic tomography methods are widely used techniques for spatial imaging of physical quantities in the crust and deeper Earth. Travel-time body wave seismic tomography is theoretically the easiest way to depict the seismic characteristics of the Earth using earthquakes (Eberhart-Phillips, 1990; Nolet, 2008; Koulakov, 2009). Many codes have been developed in the last 30 years for local earthquake tomography, providing direct-wave velocity images and allowing for testing of the reliability of the inversion process with synthetic tests and different smoothing parameters (Hansen, 1994; Kissling et al., 1994; Benz et al., 1996; Thurber and Eberhart-Phillips, 1999; Aster et al., 2005; Lees, 2007; Koulakov, 2009).

In local earthquake tomography the spatial resolution of the velocity results varies significantly due to the heterogeneous distribution of earthquake sources, the different regularization (smoothing) methodologies employed, and the non-linear scattering effects of the medium. This may create spurious phases in the waveforms, mixing their information with the ones, e.g., of the *S*-direct phases (Thurber, 1992). A flexible gridding strategy is a good technique for adapting the parameterization of a tomographic problem to an incomplete dataset, sampling only part of the medium [e.g., seismic sources only located in fault zones].

In a multi-step velocity tomography relatively high resolution can be obtained in a target area given good ray coverage, while a progressive inversion scheme can employ the results obtained in a lower resolution region (LRR) as input for the higher resolution region (HRR) (Thurber, 1987; Eberhart-Phillips, 1990; Bai and Greenhalgh, 2005; Eberhart-Phillips et al., 2008). Thurber and Eberhart-Phillips (1999) improve this scheme, combining regular gridding with two forms of node linking

* Corresponding author.

http://dx.doi.org/10.1016/j.jvolgeores.2014.03.009
0377-0273/© 2014 Elsevier B.V. All rights reserved.

to allow for finer-scale resolution where warranted by the data. Bai and Greenhalgh (2005) describe an inversion scheme of this kind, applied to velocity tomography, where rays obtained in the LRR are used to obtain the crossing points where the ray paths intersect the boundaries of the HRR, and to compute the associated travel times from regional sources to these crossing points.

Multi-resolution travel-time velocity tomography can be considered a standard seismological technique: the data are easy to retrieve and a large effort has been spent both on reducing the errors caused by the non-linearity of the inversion problem and on correctly modeling the paths followed by the *P*- and *S*-waves in the medium, generally with an infinite-frequency approximation (Dahlen and Baig, 2002; Cerveny, 2005). However, a multi-step algorithm using the results obtained in a LRR as input for the HRR is harder to design if we consider as data body-wave amplitudes instead of body-wave phases.

Today it is widely accepted that amplitude- and frequency-dependent attenuation parameters are important to characterize the physical state of a medium. The knowledge of their spatial distribution may be critical to calculating source parameters as well as for imaging fluid and melt reservoirs or for the characterization of the seismic hazard in a given region (Lees and Lindley, 1994; Quan and Harris, 1996; De Lorenzo et al., 2001; Schurr et al., 2003; De Siena et al., 2010). If a velocity structure and a ray-tracing algorithm are already available, the attenuation characteristics (i.e., the quality factor of *P*- and/or *S*-waves, *Q*) can be obtained by the measurements of direct-phase amplitudes (Lees and Lindley, 1994; Haberland and Rietbrock, 2001; Schurr et al., 2003; Koulakov et al., 2010).

In attenuation tomography the data (seismic energies or seismic amplitudes) are dependent on the source, the site, and both the elastic and inelastic propagation parameters (Del Pezzo et al., 2006; Lees, 2007; De Siena et al., 2009). Several methods have been developed to retrieve the source- and site-independent attenuation parameters from amplitude observations in highly heterogeneous media, many of them employing the effect of scattering on seismic amplitudes to remove source and site effects (Quan and Harris, 1996; Haberland and Rietbrock, 2001; Schurr et al., 2003; Matsumoto et al., 2009). However, when scattering is very strong (e.g., inside the volcanic cone) both *P*- and *S*-wave coherent information are quickly lost, and the waveforms assume diffusive characteristics (Wegler and Lühr, 2001; Wegler, 2003).

A preliminary study of the average quality factor and corresponding geometrical spreading obtained by the method is necessary for an informative interpretation of the tomographic images as well as to discriminate regions with different scattering characteristics. The trade-off between geometrical spreading and apparent quality factor stands in the way if we want to measure average and spatially dependent attenuation parameters (Morozov, 2008).

In recent years, a debate has arisen between studies considering a frequency-dependent quality factor: the standard and physically well-grounded model (Xie, 2010) contrasts with those separating the geometrical and effective attenuation, which incorporates intrinsic attenuation and small-scale scattering (e.g. (Morozov, 2008)). This last model provides a best fitting measure of the quality factor, more consistent with values obtained by laboratory experiments. In particular, geometrical attenuation is found to be positive for most waves traveling within the lithosphere; positive levels of geometrical attenuation are common in realistic, heterogeneous media, both observationally and theoretically (Morozov, 2011).

Amplitude-dependent direct-wave measurements of attenuation cannot be applied in the frequency bands where the source model is too complex (Lees and Lindley, 1994) or if the medium heterogeneity is too high (Sato et al., 2012). In a volcanic cone the high heterogeneity of the medium disrupts coherent direct-wave information after few seconds from the earthquake origin time (Wegler, 2003). In addition, frequency-dependent effects like source resonance (Chouet, 1988) or resonant scattering (Margerin, 2013) may create spurious stationary phases in the direct and coda wave-fields. These phenomena typically affect t^* attenuation measurements, widely used at local and continental scales (Lees and Lindley, 1994; Eberhart-Phillips et al., 2008).

The coda-normalization (CN) method, first developed to obtain average *P*- and *S*-wave attenuations, mixes direct- and coda-wave information, and has been used to image the attenuation structures of volcanoes at regional and local scale (Aki and Richards, 1980; Yoshimoto et al., 1993; Del Pezzo et al., 2006; De Siena et al., 2009; Matsumoto et al., 2009; De Siena et al., 2010; Sato et al., 2012). Its tomographic applications provide variations with respect to an average quality factor, and possible interpretations of the absolute spatially dependent quantities must therefore be taken with caution. The large degree of scattering and wave conversion in volcanic areas is sufficient to extend the coda normalization method to a single station measurement of *P*-wave attenuation (Yoshimoto et al., 1993).

The homogeneity of the scattering regime at a given frequency and lapse-time is the main assumption of the method, since in this case coda energy can be considered as constant. Therefore, the CN method may be used to recognize the zones with large heterogeneity, producing large scattering on the energy ratios in given frequency bands. Then, attenuation tomography can be applied with a multi-step procedure, which takes into account the different scattering characteristics of the medium in different parts of the volcanic region (De Siena et al., 2009) and tries to increase the frequency range where stable results may be obtained.

MuRAT (available at http://earth.uni-muenster.de/~ldesi_01/publications/publications.html is a Matlab© code designed to measure both the average *P*- and *S*-wave quality factors and the geometrical spreading factor. It is specifically developed for the study of highly heterogeneous areas like volcanic cones (e.g. De Siena et al., 2009) and calderas (e.g. De Siena et al., 2010), suitable both for discriminating data and regions affected by anomalous scattering and for computing correct spatially-dependent images of total direct-wave attenuation in a single linear inversion.

If anomalous scattering can be clearly related to given regions and/or surface structures, the code shows the impact of this effect on the results of the attenuation tomography at different frequencies. A mechanism of data updating increases the number of data inverted for the attenuation parameters in the regions where anomalous scattering is present. These are usually the ones both of major interest and presenting the largest velocity variations.

Here, the code is applied to two small datasets collected at Mount St. Helens and Mount Vesuvius volcanoes to obtain average- and spatially-dependent attenuation parameters for an active and for a quiescent volcano, respectively. The two tomographic analyses provide information on the level of heterogeneous scattering in these regions as well as the feasibility and effective resolution achievable by attenuation tomography in these volcanic regions.

2. Data and methods

2.1. Measurement of seismic attribute with the coda-normalization (CN) method

The CN method (Aki, 1980) is applied to the single station estimate of total inverse *P*-wave or *S*-wave quality factor (*Q*) along the *k*-th seismic path (Del Pezzo et al., 2006). The single-path attenuation is obtained in a given frequency range with central frequency f_c by measuring the direct *S*-energy, $E_k^S(f_c)$, and the coda *S*-energy from a given lapse time t_c, $E_k^C(f_c,t_c)$, and calculating their ratio (see the seismogram in Fig. 1g). The single-path CN equation is:

$$\frac{1}{2\pi f_c}\ln\left(\frac{E_k^S(f_c)}{E_k^C(f_c,t_c)}\right)=\frac{K(f_c,t_c)}{2}-\frac{\gamma}{\pi f_c}\ln r_k-\int_{r_k}\frac{dl}{v(l)Q(l)}, \quad (1)$$

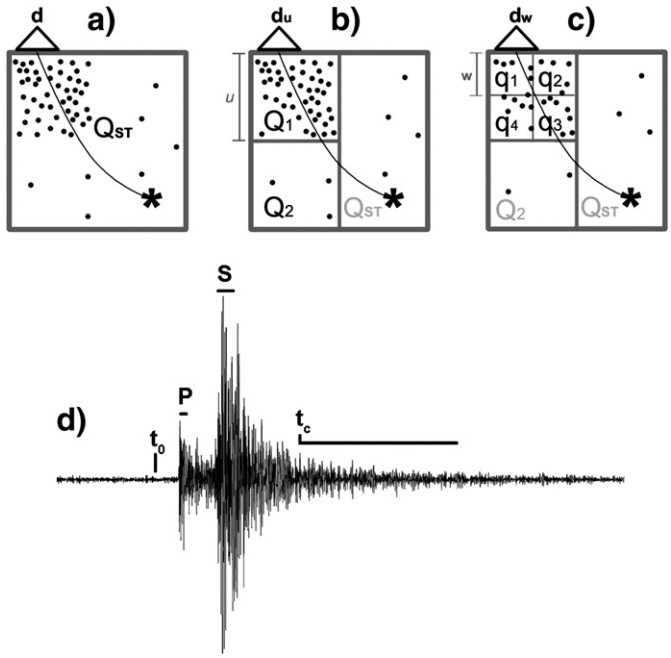

Fig. 1. a)–c) The steps of the code are sketched for a single ray crossing regions of low and high heterogeneity, where the black dots represent scattering centers. a) Both the average quality factor (Q_{ST}) and the geometrical spreading are obtained by using the entire ray. b) We solve the part of the medium where we have an adequate number of rays (we impose the blocks Q_1 and Q_2 on this region). Q_{ST} is used to update the data vector, in order to include rays which are not entirely contained in Q_1 and Q_2. c) The high resolution grid (blocks q_1, q_2, and q_3) is imposed on the regions that show strong heterogeneous scattering (higher concentration of black dots). d) A sample volcano-tectonic seismogram. We show the time windows used to compute the *P*-, the *S*- and, the coda-energy, as well as the origin time of the earthquake.

where γ is the geometrical spreading factor, $v(l)$ is the velocity measured along the ray-path, and r_k is the total length of the k-th ray. The factor $K(f_c,t_c)$ is dependent on the scattering properties of the medium and is assumed to be constant for each frequency band at a given lapse time. Introducing the slowness $s(l) = \frac{1}{v(l)}$ and discretizing, Eq. (1) can be rewritten as:

$$d_k = \frac{K(f_c, t_c)}{2} - \frac{\gamma}{\pi f_c} \ln r_k - \sum_{B=1}^{N_u} l_{kB}^u s_B^u \left(Q^{-1}\right)_B^u \tag{2}$$

where d_k is the left-hand side of Eq. (1). Index B indicates the B-th of the N_u blocks that the k-th ray crosses at resolution u. This block is therefore characterized by s_B, $(Q^{-1})_B^u$, and l_{kB} (the slowness, the inverse Q, and the length of the ray-segment crossing it). Eq. (2) can be linearly inverted for $K(f_c,t_c)$, γ, and $(Q^{-1})_B$.

2.2. The multi-step procedure

The goal of the multi-step algorithm is to improve the estimates of the model parameters (the quality factors) in regions where the scattering properties vary abruptly, or to put a constraint on the feasibility and resolution of the attenuation tomography. Fig. 1 describes the way the multi-step code acts for a single ray following an infinite frequency approximation (Dahlen and Baig, 2002; Nolet, 2008) and crossing a region with different scattering characteristics, as a volcanic cone or its feeding system.

In Fig. 1a the average Q (hereafter called Q_{ST}) is calculated with the corresponding geometrical spreading. In Fig. 1b a low resolution grid of step u is imposed without including the entire ray, in order to consider, e.g., regional seismicity far from the highly-heterogeneous volcanic edifice and feeding system. Q_{ST} and the geometrical spreading factors are used to update the data vector at resolution u (d_u). The results at resolution u can be computed together with the geometrical spreading if the seismicity homogeneously samples the medium, with no evidence of strong spatially-dependent and frequency-dependent heterogeneous scattering affecting coda waves (e.g. De Siena et al., 2010).

In the final step we impose a grid of step $w \leq u$ on the volumes that cause a systematic change in the linear relationship with time defined by Eq. (2) (Fig. 1c, high concentration of scattering centers, black dots). Q_{ST}, the geometrical spreading factor, and the results obtained at resolution u are used to update the data vector d_w in a second-step inversion, where the parameter models are the variations of the inverse quality factors in the blocks of the grid of step w. We apply both the single-step and the multi-step algorithms to the Mount St. Helens dataset, where spatially-dependent and frequency-dependent heterogeneous scattering corrupts the linear relationship with time shown by Eq. (2).

The three average quantities ($K(f_c,t_c)$, γ, and $Q^{-1} = Q_{ST}^{-1}$) are obtained with a simple least squares approach assuming an average velocity by using Eq. (1). The covariance matrix is used to assign an uncertainty to each of the parameters. The values of $K(f_c,t_c)$ and γ are stored for the following steps. The energy ratio and the average quality factor with corresponding standard deviations are finally plotted to show the fit with the data.

The second inversion problem provides an image of the attenuation parameters Q_B^{-1} in a grid of u meters cell size. The inversion provides the variations with respect to the average quality factor in the ray geometry of the first inversion problem, for blocks of u meters side:

$$d_k^u = \sum_{B=1}^{N_u} l_{kB}^u s_B^u \left[\left(\delta\left(Q^{-1}\right)^u\right)_B\right] = \sum_{B=1}^{N_u} G_{kB}^u \left[\delta\left(Q^{-1}\right)_B^u\right] \tag{3}$$

where the elements of the inversion matrix, G_{kB}^u, are the length of the k-th ray segment in the u-meter side B-th block, l_{kB}^u, multiplied by its slowness s_B^u (De Siena et al., 2009):

$$G_{kB}^u = l_{kB}^u s_B^u. \tag{4}$$

The new data vector d_k^u is:

$$d_k^u = -d_k + \frac{K(f_c, t_c)}{2} - \gamma \ln r_k - \sum_{B=1}^{N_u} l_{kB}^u s_B^u Q_{ST}^{-1}. \tag{5}$$

Therefore, the total quality factor in each block B is:

$$Q_B^{-1} = Q_{ST}^{-1} + \delta\left(Q^{-1}\right)_B^u. \tag{6}$$

With this notation, keeping the geometrical spreading constant, we assume that the quality factors are a measurement of both intrinsic and scattering effects (Morozov, 2008; Xie, 2010). The problem is solved separately for each frequency band with a damped least-squares method (zero-order Tikhonov regularization – e.g., Aster et al. (2005, chapter 5)). The damping parameter can be automatically chosen from the L-curve representing the log–log plot of the norm of a regularized solution versus the norm of the corresponding residual norm; however, the user may choose different damping parameters for the further assessment of the results. The singular values from the singular value decomposition of the G matrix are also plotted at each tomographic step (Hansen, 1994).

In the presence of high quality data homogeneously sampling the region and in the absence of strong heterogeneous scattering a single linear inversion is sufficient (De Siena et al., 2010). However, the study of the energy ratios with travel time may highlight zones of anomalous scattering, where the scattering or source model abruptly changes, affecting the measured data (which are normalized for a coda wavefield which is assumed as constant) as well as the uncertainties associated with the measurements. Under a volcanic cone this region is

usually the one where the seismic sources are clustered. A second inversion problem may be defined (w-meters) where the model space changes and the results of the first inversion are used as data (Fig. 1c).

The element of the data vector for the k-th ray crossing the N_w blocks is:

$$d_k^w = -d_k + K(f_c, t_c) - \gamma \ln r_k - \sum_{b=1}^{N_w} l_{kb}^w s_b^w Q_B^{-1}, \tag{7}$$

where $[Q_B^{-1}]$ is the value of the quality factor measured in the previous inversion and also characterizing the smaller w-meter block (Fig. 1). Hence, the inversion problem becomes:

$$d_k^w = \sum_{b=1}^{B_w} G_{kb}^w \left[\delta\left(Q^{-1}\right)_b^w\right] \tag{8}$$

where the superscript w stands for the step of the grid and the $(\delta Q^{-1})_b^w$ are the variations with respect to the inverse quality factor of the u meter cube in which they are contained. The elements of the inversion matrix, G_{kb}^w, are the lengths of the k-th ray segment in the w-meter side b-th block l_{kb}^w multiplied by its slowness s_b^w:

$$G_{kb}^w = l_{kb}^w s_b^w. \tag{9}$$

The inversion is linear and the P- and/or S-inverse quality factor of each w meter block b is given by:

$$q_b^{-1} = Q_B^{-1} + \delta\left(Q^{-1}\right)_b^w. \tag{10}$$

The solution in a single- or double-step tomographic model is to be interpreted with caution. Factors like wavelength and source oversampling, and/or ray-path under-sampling heavily affect the problem, causing unstable and non-unique solutions. The resolution, stability, and robustness of the results must be checked by using bootstrap, checkerboard, and synthetic anomaly tests, by looking at the covariance matrix, or by varying the smoothing parameters (Hansen, 1994; Aster et al., 2005; Lees, 2007; Koulakov, 2009, 2013).

An additional tool of MuRAT is a simple checkerboard test, which is performed at each step of the tomographic inversion, and which can be compared with the diagonals of the resolution matrix of the model parameters. The input of the resolution test is a checkerboard structure with large anomalies (cubic blocks of side $2u$ meters). Smaller anomalies, e.g., of the order of the resolution obtained from the inversion, will be poorly resolved and may provide an underestimation of the effective smearing affecting the images, depending on the ray-path geometries and on the frequency content (Koulakov, 2009; De Siena et al., 2010; Koulakov, 2013). We use blocks with quality factors respectively equal to 100 and 1000, respectively, as input. The presence of fluids, melt, or gases can strongly increase attenuation, hence P- and S-wave Q values as low as 10 or less are not uncommon in attenuation tomography results (Schurr et al., 2003; Lees, 2007; De Siena et al., 2010).

2.3. The two sample applications

P- and S-wave velocity tomography and accurate locations of seismic events have been obtained by the application of travel-time tomography on passive seismic datasets both at Mount St. Helens (MSH) volcano (Lees, 1992; Moran et al., 1999; Waite and Moran, 2009) and at Mount Vesuvius (MV) volcano (Scarpa et al., 2002). A sample earthquake (star) with the corresponding seismograms at different stations is plotted for each volcano in Figs. 2b and 3b, respectively.

We set the time window used to measure P- or S-energy on both datasets to 1 s, in order to average our measures for radiation pattern effects (De Siena et al., 2009) and choose three different frequency bands: 3 Hz, 6 Hz, and 18 Hz (Tusa et al., 2004; De Siena et al., 2009). This last choice theoretically leads to a maximum resolution of approximately 1 km in each area, considering the average velocity of P-waves at MSH (Waite and Moran, 2009) and of S-waves at MV (Scarpa et al., 2002).

2.3.1. Mount St. Helens (MSH)

MSH is an active volcano, which has erupted several times in the last four decades (see Sherrod et al. (2008) for a description of its eruptive history) and a large number of earthquakes have been recorded under the volcano and along the surrounding fault systems (e.g. Waite and Moran, 2009). The rays used in the MSH example were calculated with a Thurber modified approach (Block, 1991) using the P-wave velocity model obtained by Waite and Moran (2009). This velocity model depicts the velocity structures in a volume of $40 \times 40 \times 25$ km centered at MSH. It has been cubic-interpolated at 0.75 km.

The 451 vertical-component waveforms used in this study were retrieved from the IRIS facilities, where they have been stored from the PNSN network – Washington Cascades, for the period 2000–2003, prior to its most recent eruption (October 2004). The stations are shown in red if they are located on or near the volcanic edifice (red triangles and names, Fig. 2a) in gray otherwise. The seismicity is located below the cone, between depths of 2 and 11 km (red dots, Fig. 2a) and along the nearby faults, generally at greater depths (black dots).

All the vertical recordings used in this study show a clear P-wave onset and are considered by Waite and Moran (2009) to be of volcano-tectonic type. During the period 2004–2008 several low-period and very-low period resonant earthquakes were located inside the MSH cone (e.g. Waite et al., 2008). These earthquakes produce a resonant signature, which affects direct and coda waves in the 3 Hz frequency band. We only consider earthquakes located below 2 km depth under the MSH cone in order to avoid this signature, which could influence the attenuation measurements at 3 Hz and (less evidently) at 6 Hz (Waite et al., 2008).

Between 2000 and 2003 the seismicity had an average depth of 2.5 km, with very few earthquakes located between depths of 0 and 2 km and a few larger events at greater depths (Waite and Moran, 2009). The reawakening of MSH in 2004 was surprising because the preceding 4 years had seen the fewest earthquakes since the 1980–1986 eruption ended. This pattern suggests that there was no movement of fluids of melt under the volcano until 2004 (Sherrod et al., 2008). The 2000–2003 time period is well separated from the eruption period (September 2004), hence we assume that the attenuation parameters are constant with time.

2.3.2. Mount Vesuvius (MV)

We use 105 three-component waveforms recorded between 1999 and 2000, located inside the volcanic edifice of MV (Fig. 3) and provided by the INGV – Vesuvius Observatory. This is just a subset of the waveforms that have been used in two other studies to image the attenuation structure at MV with the CN method in different frequency bands (Del Pezzo et al., 2006; De Siena et al., 2009). The Thurber-modified ray-propagator calculates rays by using the S-wave velocity model obtained by Scarpa et al. (2002). The velocity model has an average resolution of 0.9 km and it covers a volume of $10 \times 10 \times 10$ km centered under the central cone of MV.

MV is a quiescent volcano, its last eruption dating to 1944 (Marianelli et al., 1999). The recurrent low-magnitude volcano-tectonic seismicity shows fault-plane solutions in good agreement with the regional tectonics (Scarpa et al., 2002). If we compare the average direct-wave quality factors obtained by using data recorded before [January–December 1996, Bianco et al. (1999)], during, and after 1999 [1999–2006 (De Siena et al., 2009)] we observe a small increase of the attenuation parameters. However, the increase is much smaller than the uncertainties related to the attenuation parameters. Therefore, we assume that the attenuation parameters are constant with time, as at MSH volcano.

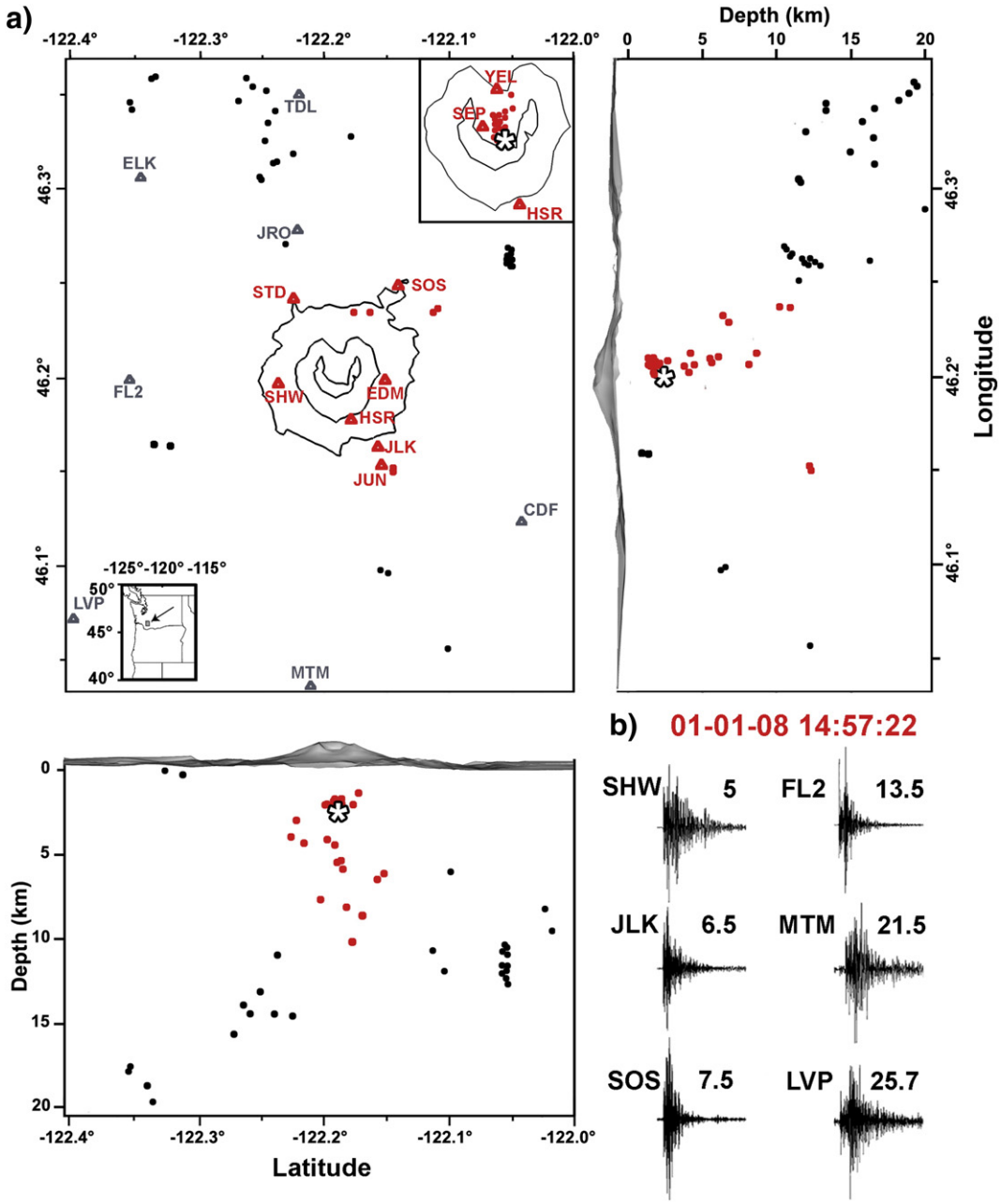

Fig. 2. a) A subset of the permanent PNSN network stations located at MSH in the period 2000–2003 (triangles and names) with the corresponding seismicity (dots). We only plot a contour map of the cone for altitudes above 1700 m. The zero of our Cartesian reference system is at latitude −122.2° and longitude 46.2°. Inset in the lower left and upper right corners show the location of MSH in southern Washington and a close up of the crater, respectively. The star represents the location of the example source used to show the effects of the medium on the recorded amplitudes. Red sources recorded at red stations are characterized by anomalous behavior of the energy ratios with increasing *P*-wave travel times. b) We show six vertical component velocity seismograms recorded at difference distances from the example source (star, panel a). The origin date and time are shown above the seismograms whose duration is 50 s. The name of the station and the ray length (in km) are shown near each seismogram.

3. Results

The dots in both Figs. 4 and 5 show the logarithm of the *P*-wave or *S*-wave energy ratios divided by $2\pi f_c$ (that is, the left-hand side of Eq. (1)) versus the direct-wave travel times. In the same figures the right-hand side of Eq. (1) (obtained from the weighted least squares inversion for the three average parameters) is shown as continuous lines of different colors. If the CN model is valid both the right-hand side and left-hand side of Eq. (1) show a negative linear relationship with the direct-wave travel times.

We show these plots for *P*-waves at MSH (Fig. 4) and for *S*-waves at MV (Fig. 5) in the 3 frequency bands considered before by, e.g., Tusa et al. (2004) and De Siena et al. (2009). In the case of MSH we show the results of the inversion both of the entire dataset (cyan dots and cyan line) and of data corresponding to *P*-wave travel times smaller than 2 s (red dots and red line). In Figs. 4 and 5 the uncertainties on the parameter models are obtained by using the covariance matrix and shown for the inversion of the entire dataset only. These plots are used to discriminate zones of ray trapping, anomalous scattering, and source incorrect modeling which typically characterize direct- and coda-waves in volcanic regions (Neuberg and Pointer, 2000; Chouet, 2003; Parsieglia and Wegler, 2008; De Siena et al., 2013).

The logarithms of the *S*-coda energy divided by the noise energy versus the lapse times are also provided by the code and help decide the

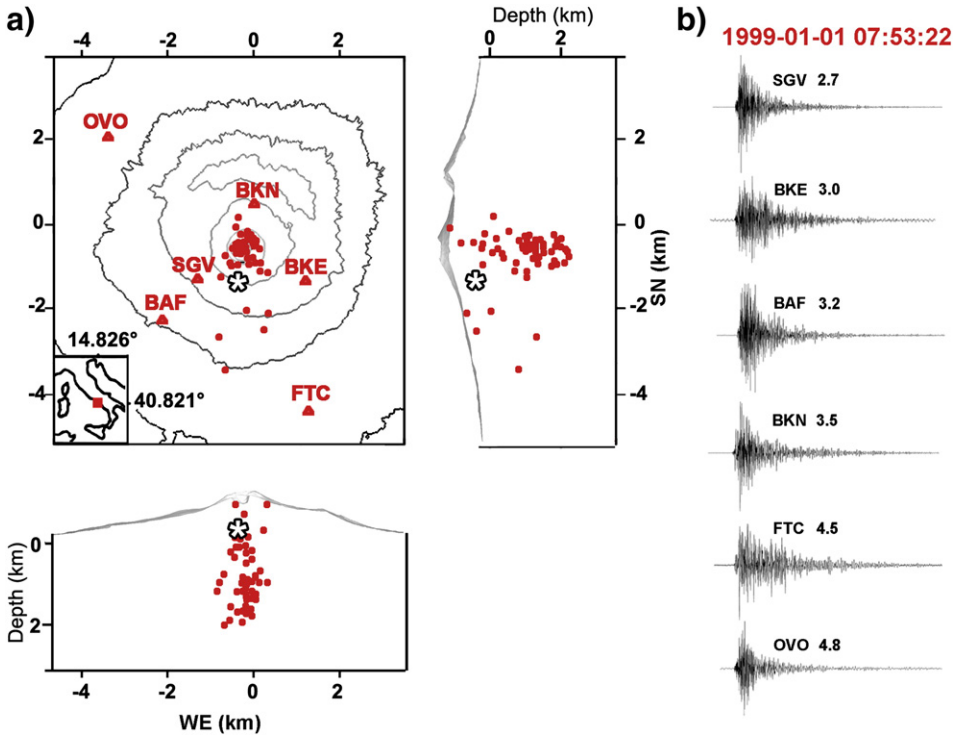

Fig. 3. a) A subset of the permanent and mobile stations (red names and triangles) located at MV in the period 1999–2001 with the corresponding seismicity (red dots) plotted on topography contoured at 500 m intervals. Inset in the lower left corner shows the location of MV in Italy (red square) and the coordinates of the zero of our reference system. The star represents the location of the example source used to show the effects of the medium on the recorded amplitudes. b) We show six seismograms recorded at difference distances from the example source (star, panel a). The origin date and time are shown above the seismograms whose duration is 45 s. The name of the station and the ray length (in km) are shown near each seismogram.

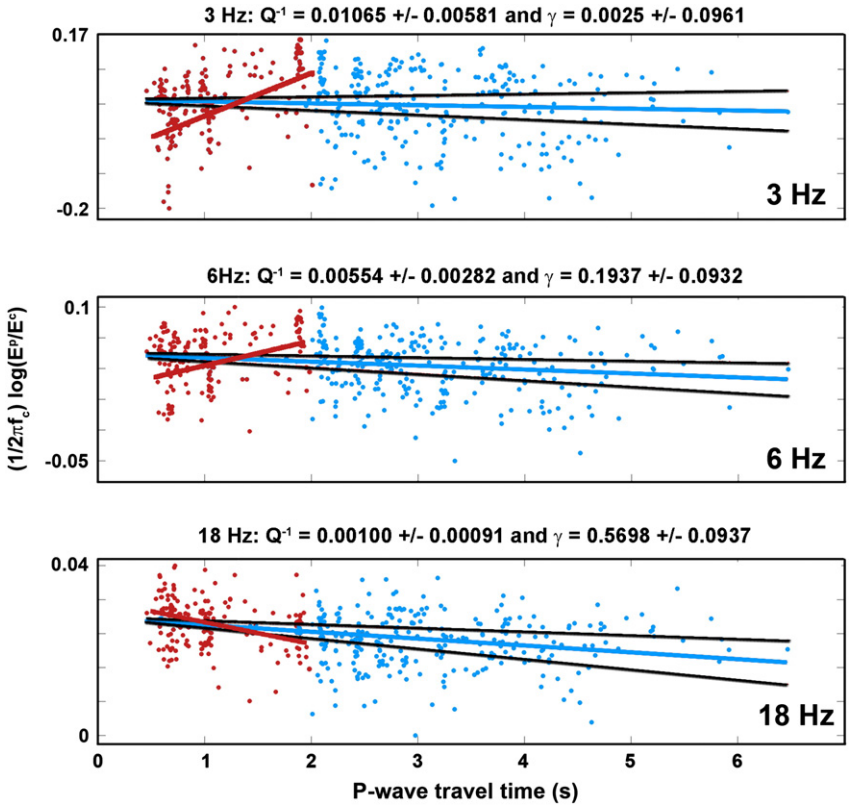

Fig. 4. A plot of the logarithm of the *P*-wave direct-to-coda energy ratios divided by $2\pi f$ (red and cyan dots, computed at MSH in three frequency bands) versus the *P*-wave travel times. The values shown by the red dots are produced by red earthquakes and recorded at red stations in Fig. 2a. The red lines show the linear fit that would be obtained by using only the data between travel times of 0 and 2 s, and which would give a negative inverse-Q. The cyan lines represent the least squares fit to the model parameters by using the entire dataset. The maximum uncertainties corresponding to the model parameters are obtained by using the covariance matrix (black lines). The geometrical spreading and the average *Q* obtained from the inversion for the average parameters are shown above each plot.

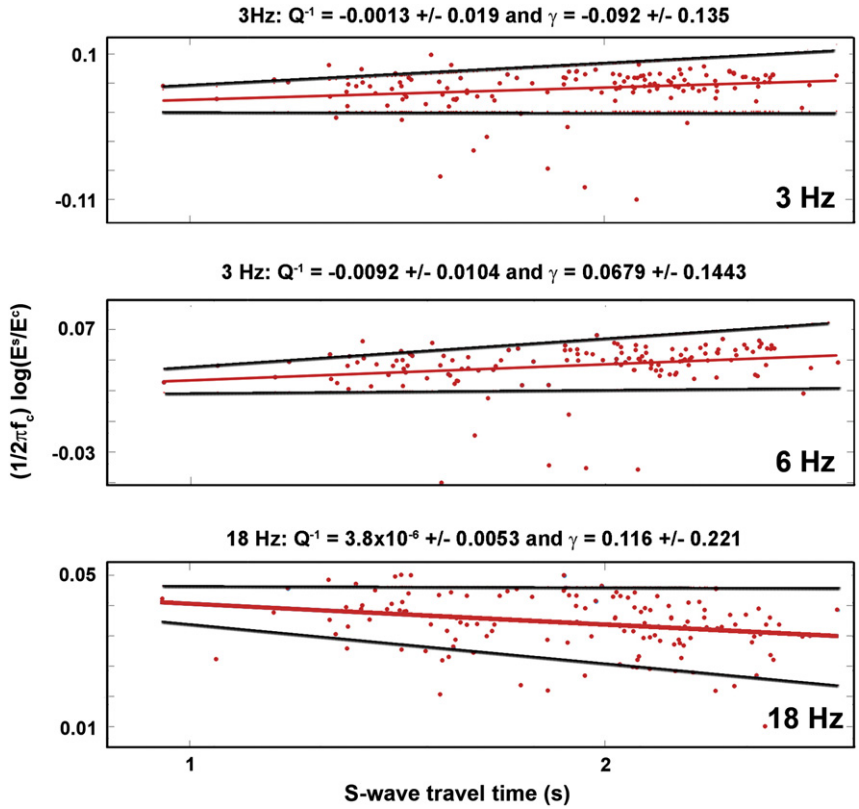

Fig. 5. Same as Fig. 4 for *S*-wave measurements at MV. The data are only available at *S*-wave travel times between 0 s and 2.5 s. We use the fit to these data (red line) to show the similarity between these observations and the ones at short travel times in Fig. 4.

maximum lapse time at which we still observe coda waves. It is important to set large values of the lapse time to avoid the transient regime: the lapse time assumed in literature (twice the *S*-wave travel time) is usually too short in highly heterogeneous areas (Wegler and Lühr, 2001; Sato et al., 2012; Calvet and Margerin, 2013).

We define t_c as the starting time for the coda window (Fig. 1) and set it at 15 s for both MSH and MV. In the weighted least squares inversion for the average attenuation parameters the code assigns a lower weight to data that have a low coda-to-noise ratio. After a lapse time of $t_c = 25$ s less than 10% of the coda measurements have a signal-to-noise ratio lower than 2 in the 3 Hz and 6 Hz frequency bands for both datasets. Therefore, the total coda duration t_w is set to 10 s, with lower weights assigned to data having coda-to-noise ratios lower than 2.

3.1. Average attenuation and scattering parameters at MSH

Fig. 4 (dots) shows the travel-time dependence of the logarithm of the *P*-wave energy ratios on travel time at MSH. The parameters obtained by using data that span the entire region are shown above each plot.

The coefficient of the *P*-wave geometrical spreading increases with frequency, however, it does not reach a value comparable with the one associated with body-wave amplitudes in a homogeneous spherical Earth (e.g., Lay and Wallace, 1995, pag. 94). As the frequency increases (Fig. 4, 18 Hz) the red trend (obtained by using data corresponding to *P*-wave travel times smaller than 2 s) fits the cyan linear trend better, while the uncertainties associated with the Q estimates (black lines) decrease. The source-station paths related to the red energy ratios and the corresponding red trend are mainly produced by the red-colored sources and recorded at the red-colored stations in Fig. 2a.

The MSH heterogeneous cone produces reflectivity, resonance, and interference effects which act differently for different frequency bands (Chouet, 2003; Morozov, 2011; De Siena et al., 2013; Margerin, 2013) and may enhance coda energies at short lapse times, that is, for the seismicity produced under the cone (Fig. 2a, red dots). The corresponding energy ratios, measured between *P*-wave travel times of 0 and 2 s, do not agree with the linear decrease that characterizes the energy ratios between 2 s and 7 s both at 3 Hz and 6 Hz (Fig. 4, 3 Hz and 6 Hz). If we consider the 0 to 2 s travel-time interval only we obtain a negative *Q*.

These differences in geometrical spreading and in the values of the total quality factor can be explained by the presence of strong lateral variations in the velocity and scattered wave-field at regional scale, induced by the feeding system of the volcano (Wegler and Lühr, 2001; Wegler, 2003; Waite and Moran, 2009). These variations and the enhanced reflectivity from the cone cause interference and narrow-band resonance effects that may increase coda energy, decrease direct energy, and consequently decrease the energy ratios (Morozov, 2011; De Siena et al., 2013; Margerin, 2013). These observations are not accounted for by travel-time tomography, which must assume smooth variations of the velocity wave-field in the entire region (Waite and Moran, 2009).

The vertical seismograms in Fig. 2b are corrected for the instrument response function. They provide direct information on lateral differences in seismic attenuation which cannot be modeled as a simple 2D layered structure. As an example, the *P*-waveform similarities at small distances, e.g., between stations SHW and JLK, ensure that radiation pattern effects are spatially homogenized after a few seconds from nucleation. *S*-coda behaviors are instead strongly affected by the station location with respect to the volcanic cone, with larger coda energy at larger lapse times for station SHW. The 3D heterogeneous structure of the region produces strong effects on the coda wave-field, which are not modeled by homogeneous scattering.

We obtain the attenuation images by using data filtered in the 6 Hz frequency band, where the coefficient of the geometrical spreading is $\gamma = 0.1937 \pm 0.0932$. We cannot completely ensure the absence of resonant low-period sources in our dataset, even if we selected a subset of volcano-tectonic earthquakes already used by Waite and Moran

(2009). Nevertheless, we assume that direct- or coda-observations are less affected by source resonance in this frequency range (Chouet, 2003; Waite et al., 2008). We also note that eventual surface-wave energies contained in the coda time-window could be responsible for the low geometrical spreading factors, at least at 3 Hz and 6 Hz (Yamamoto and Sato, 2010).

In our interpretation, the differences between the cyan and red fits in Fig. 4 at 3 Hz and 6 Hz are correlated with a spatial increase in the heterogeneity of the medium which mainly affects low frequencies. This is supported by the results of Tusa et al. (2004). These authors obtain source parameters of micro-earthquakes located at MSH between 1995 and 1998. When they try to correct for *P*-wave attenuation they have to divide the 2–7 Hz frequency range from the one above 15 Hz to account for a spectrum lacking corrected spectral amplitude values. Our results indicate that this effect is enhanced by the division of direct-wave energy by coda energy.

3.2. Average attenuation and scattering parameters at MV

We confirm anomalous behavior of the energy ratios at short direct-wave travel times (between 0 and 2 s) for earthquakes located inside a volcanic cone and for *S*-waves by looking at the results of the analysis of the average parameters at MV (Fig. 5). In this case, the travel times only span 3 s and the stations are mostly located on the volcanic edifice (Fig. 3).

The geological setting as well as the scale of the systems are different; at MV only the volcanic cone and the 3 km underneath are sampled by the rays, while at MSH a much wider and deeper volume is sampled. The anomalous heterogeneous scattering inside the cone produces non-physical negative inverse Q and/or negative geometrical spreading at MV (Fig. 5). A positive average Q is only obtained at 18 Hz. By using only the seismicity confined inside the cone or underneath, at travel times between 0 and 2 s (Figs. 4 and 5, red dots), we get similar behavior of the energy ratios in the two volcanic areas.

Both a positive physically-related Q and a positive geometrical spreading can only be obtained with data sampling the cone laterally and at depth, as at MSH. In the case of MV, the coda-normalization method can only be applied in the highest frequency band [18 Hz, see De Siena et al. (2009)] if we consider a short *P*- or *S*-wave direct window, where coherent information is still present. However, a direct time window large enough to smooth the source radiation pattern is also necessary for the application of the coda-normalization method (Del Pezzo et al., 2006; De Siena et al., 2009) and a compromise between this effect and the quick loss of coherency must be found.

The application of diffusive techniques using only the incoherent part of the seismogram is a safer strategy to quantify the attenuation parameters in the cone (Wegler, 2003). Incoherent reflectivity leads to geometrical-attenuation coefficients which are proportional to the mean squared reflectivity. Hence, positive levels of geometrical attenuation (negative γ, Fig. 5) are common in realistic, heterogeneous media, and can be compared for different volcanic regions (Morozov, 2011).

In our interpretation the results at MV show that anomalous concentration of energy affects the waveforms produced inside the cone, and that resonance may be induced by the presence of strong lateral variations in the velocity field (De Siena et al., 2013; Margerin, 2013). We infer that the red positive trends at 3 Hz and 6 Hz in Figs. 4 and 5 are induced by a systematic error in either the CN method or, more generally, the ray approximation. This error is due to physical processes underestimated by the homogeneous scattering approximation (the basal assumption of the coda-normalization method) and causing a quick loss of direct-wave coherency.

3.3. MSH attenuation tomography with an undersized dataset

In Fig. 6a we show two tomograms obtained at 6 Hz at MSH with a single- and double-step tomographic inversion. The zero-order Tikhonov inversion approach uses the codes developed by Hansen (1994) to solve both inversion problems. The MuRAT code shows the amount of smoothing required to obtain stable solutions as well as the effective number of blocks which can be solved at each step of the inversion. The smoothing parameters can be decided by the operator and an analysis in terms of these parameters is necessary for the assessment of the results, and for a better interpretation of the anomalies.

We use a double-step approach imposing a second grid including both the red-colored stations and the red-colored seismicity of Fig. 2a down to a depth of 8.5 km. Our aim is to compare the stability and resolution of the single-step and double-step inversion results. We will derive information both on the maximum resolution achievable with the current dataset and on the effect of the systematic non-linear behavior on resolution at short travel times by the comparison of the checkerboard tests with the diagonal values of the resolution matrices.

The attenuation parameters are distributed on a grid of 2 km step defined between the surface and 25 km. Fig. 6a shows a vertical slice crossing the cone through the results of the single-step (left) and double-step (right) inversions, where the limits of the second grid are contoured with a red line. The black line shows the volumes of high resolution for velocity tomography (Waite and Moran, 2009).

The comparison between the tomograms of Fig. 6a shows a general increase in the attenuation parameters in the double-step inversion results with respect to those in the single-step inversion in the region contoured with the black line. The smoothing parameters (α) provided by the L-curve for the two inversions are $\alpha = 0.28$ (single-step) and $\alpha = 0.016$ (double-step) Fig. 6b.

The results of the single-step inversion show high attenuation between the surface and a depth of 8 km the cone and between depths of 0 and 6 km west of it. The results of the double-step inversion show instead that only the cone and the first 8 km underneath are characterized by attenuation much higher than the rest of the medium, particularly the eastern part of the cone. If we compare the double-step inversion results with the velocity tomograms of Waite and Moran (2009), the cone appears as a spot of high total attenuation and low velocity in the center of the medium.

The high-resolution velocity results in this depth range show low velocities corresponding to a shallow magma and fluid storage zone under the cone only, with its lower boundary at high-velocity igneous intrusives (Waite and Moran, 2009) while high attenuation generally characterizes both the cone and the 8 km underneath. The dataset presented here is too small for a tomographic study of the entire region. However, the double-step high attenuation anomaly better correlates with low velocity anomalies: in our interpretation, the double-step high attenuation anomaly is more realistic and informative than the laterally extended high-attenuation anomaly obtained from the single-step inversion.

3.3.1. Stability tests at MSH

As a test of the stability of the single- and double-inversion problems we use the discrete Picard condition (see Hansen (1994) for a complete reference). After a singular value decomposition of the inversion matrix MuRAT provides diagrams that compare the singular values with the dot product of the columns of the matrix spanning the data space and the data vector (Fig. 6c).

In the single-step case 50% of the dot products decay to zero more quickly than the singular values (compare the red and black trends in Fig. 6c): the under-determined problem (1250 parameter models *M*, Fig. 6c) is strongly unstable. The singular values decrease abruptly after 250: the most unstable results are obtained below the cone, where the CN model is clearly affected by a systematic error (Fig. 4, 6 Hz, red trend) but where we also expect higher resolution due to higher ray crossing (Fig. 7).

The Picard plot for the double-step second inversion (Fig. 6c) shows that 16% of the dot products decay to zero more quickly than the singular values. This is a direct consequence both of the reduction in the number of parameter models (which could have been achieved by a simple

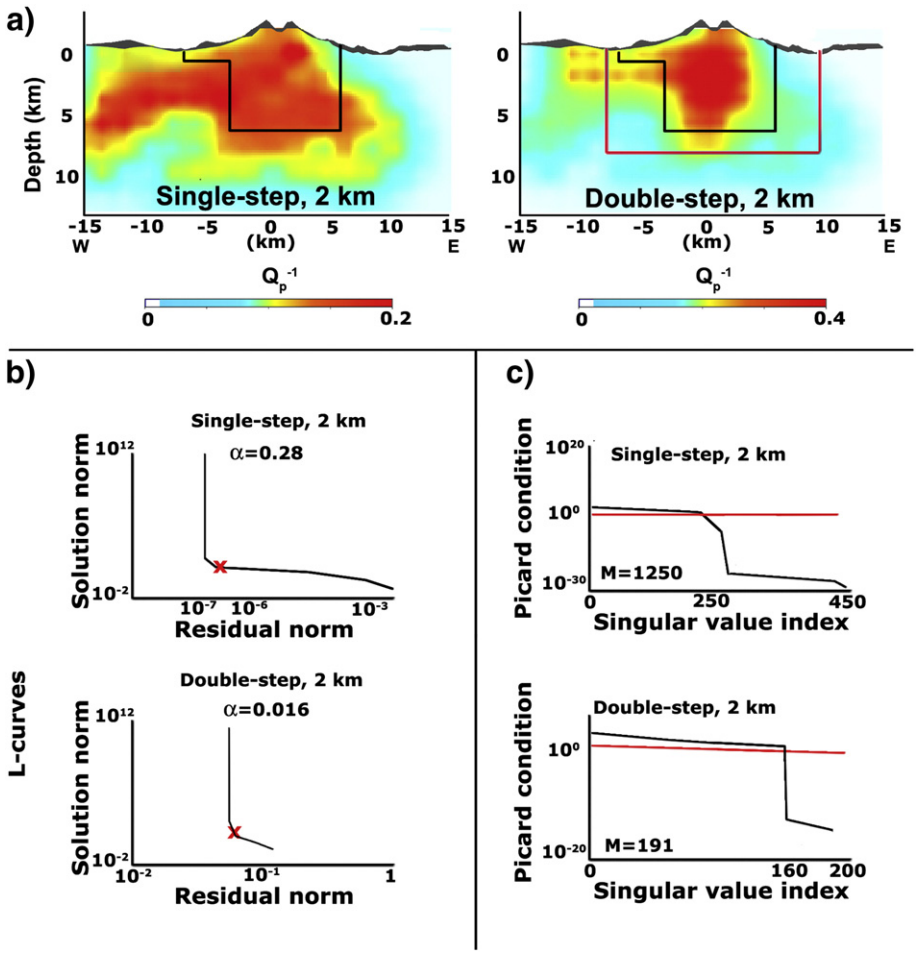

Fig. 6. a) A vertical slice through the result of the single-step (left) and double-step inversions (right) for the *P*-wave attenuation structure at MSH at 6 Hz. The black line contours the regions described in the text, defined after considering the ray geometry of Waite and Moran (2009). The red line in the right-hand tomogram contours the regions on which the second grid has been imposed. b) The L-curves and the smoothing parameters (α, red crosses) associated with each regularized inversion by the code. c) The Picard plots corresponding to each regularization (Hansen, 1994). The red continuous lines represent the singular values. The black lines show the decrease in the dot product of the columns of the matrix spanning the data space and the data vector. We also show the number of parameter models solved by the inversion.

single-step inversion in the second grid) and of the preservation of the number of data still considered in the inversion (as a direct consequence of the double step algorithm we still use the 87% of our original energy ratios).

In a direct single-step inversion for the attenuation parameters contained in the second grid we cannot consider waveforms that originated outside of the grid itself: in our particular case, this reduces the number of useful data to 41% of the total and affects the stability of the final result. By simply adding sources located inside the grid (e.g., inside the cone) we risk instead to diverge even more from the CN relationship (as it will be shown in the MV example) increasing the instability of the solution.

3.3.2. Resolution tests at MSH

We investigate whether the introduction of the second grid is correlated with a change in resolution by comparing the results of a checkerboard test with the diagonals of the resolution matrix in the two cases (Fig. 7). We directly compute the resolution matrix of the Tikhonov regularization by using the corresponding filter functions since the number of data in the inversions is small. This computation becomes very time-consuming for larger datasets: the generalized cross-validation method is a much more effective method for the stochastic estimation of the model resolution matrix by using larger datasets (MacCarthy et al., 2011).

The single and double-step approaches are tested with the corresponding checkerboard tests (Fig. 7a). Each of the cubic anomalies (defined between the surface and 25 km) has side 4 km. If we consider our ray geometry (similar to the one of Waite and Moran (2009)) the region possibly interpretable is the one below the cone (contoured with a black line in Fig. 7a,b) down to a depth of approximately 6 km. This region shows large smoothing effects in both inversions (Fig. 7a).

By inverting the data in a single-step none of the high-attenuation anomalies may actually be reconstructed. On the other hand, if the double-step checkerboard test produces high attenuation anomalies at depths greater than 0 km which may coincide with the input in some case, these anomalies do not define a clear checkerboard pattern. The comparison between the checkerboard test and the Picard condition shows that the stability of the solution inside the second grid increases, while the resolution in the same volumes remains apparently poor.

A second way to assess the effective resolution of our images is to compare the checkerboard test outputs with the diagonal of the resolution matrix. In Fig. 7b we associate to each solved block the corresponding element of the diagonal of the resolution matrix (D) associated with the Tikhonov regularization. The diagonals of the single-step resolution matrix (Fig. 7b, upper tomogram) show values around 0.8 in the region contoured with the black line between depths of 0 and 5 km. This values increases to 0.9 when we perform a double-step inversion (Fig. 7b). The comparison between the single-step and double-step results shows a

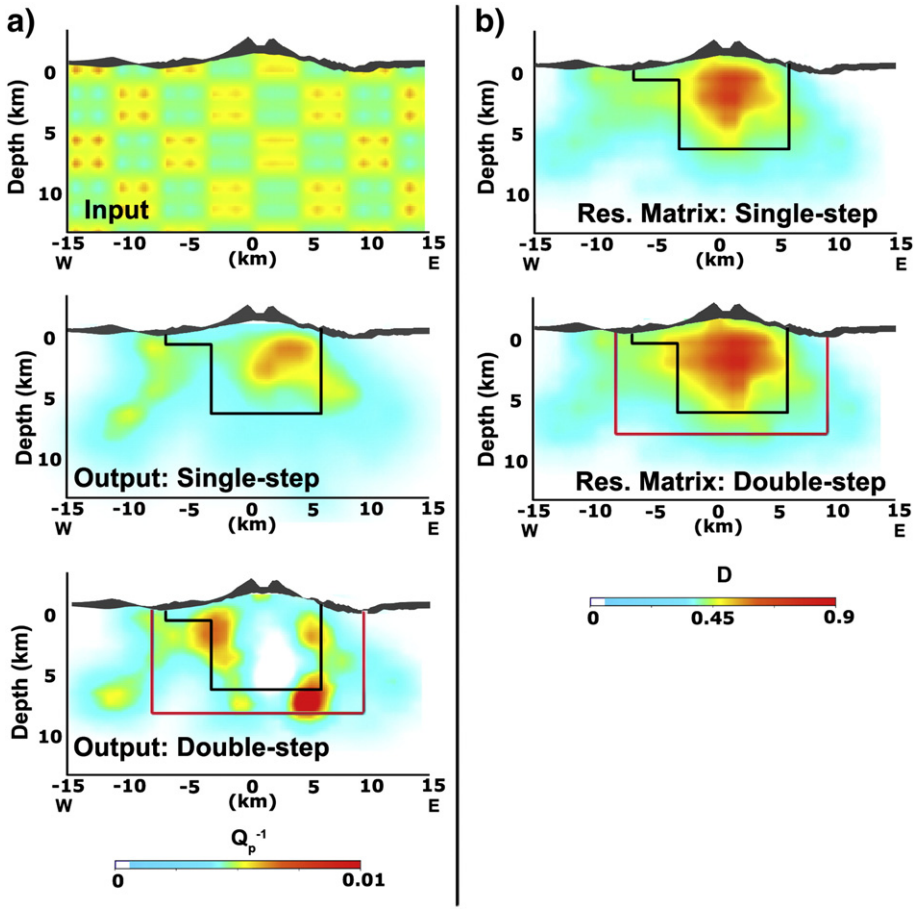

Fig. 7. a) The input as well as the outputs of the synthetic test for the single- and double-step inversions. The red line in the lowest tomogram contours the regions on which the second grid has been imposed. The black lines contour the regions described in the text, defined after considering the ray geometry of Waite and Moran (2009). b) The diagonal elements of the resolution matrices defined by using the filter functions associated with the singular value decomposition of the single- and double-step inversions (chapter 5 Aster et al., 2005).

slight increase in the values of the diagonal element of the resolution matrix in the second case.

The increase in resolution due to the double-step approach is actually very small (Fig. 7). However, if we consider the increase in both the number of data and stability that the regional seismicity may provide at MSH, paired with a slight increase in resolution, we infer that the double-step approach is more apt to reproduce total attenuation anomalies at MSH in the 6 Hz frequency range.

3.4. MV attenuation tomography with a spatially biased dataset

A typical strategy to increase resolution in a given part of a tomographic model is to increase the number of data that originated in the region. At MSH this means adding data and inverting for the attenuation parameters in the second grid only. Through the application of the CN method to MV we show how this distribution of seismic sources and stations produces bias in the results of a single-step attenuation tomography. As remarked in the previous sections we obtain a positive *S*-wave quality factor at 18 Hz only (Fig. 5), hence, we can only apply the CN method in this frequency range (De Siena et al., 2009). The large number of volcano-tectonic earthquakes located in the cone theoretically provides a sufficient amount of data to solve for the cone attenuation structure at good resolution at 18 Hz.

Unfiltered waveform data recorded at different stations at MV are plotted with respect to the ray distance in Fig. 3b. The source-station direct and coda energies are the average of the energies measured on the three velocity components. The ray distances vary much less at MV compared with those at MSH since the seismic stations are only distributed on the volcanic cone and its nearer surroundings. Most of the seismograms show missing *S*-onsets, a long coda, and a diffusive shape.

These shapes are similar to the ones observed by Wegler (2003) at stations located on the volcanic cone by using active seismicity. The *S*-onset is clearer for stations far from the cone (e.g., station OVO, Fig. 3b), which do not interact with the cone structure. Hence, we assume that the nature of the seismicity does not affect the attenuation measurements.

We use a single-step inversion at 0.9 km cell size and at 18 Hz, and we show the change produced by the smoothing parameters on the final images and the corresponding resolution tests, having input anomalies of 1.8 km dimensions. The parameter provided by the L-curve analysis ($\alpha = 128$) is also changed to $\alpha = 7$ following the discrepancy principle (chapter 5 Aster et al., 2005). From the comparison of the images obtained by using different α we can clearly see that the level of smoothing assigned by the code is too elevated to image any attenuation contrast ($Q = 100$ and $Q = 1000$ in the input of Fig. 8a).

The poor resolution is due to the incorrect behavior of the L-curve associated with the inversion problem (Fig. 8b), which does not present a typical L-shaped kink. The L-curve routine (Hansen, 1994) is not apt to reproduce the correct amount of smoothing required for the inversion. However, even if we use the discrepancy principle (Fig. 8c), which lowers the smoothing coefficient to $\alpha = 7$, we may safely infer that the smaller high attenuation anomalies produced by the inversions are artifacts. Lowering this value only increases instability without having effects on resolution.

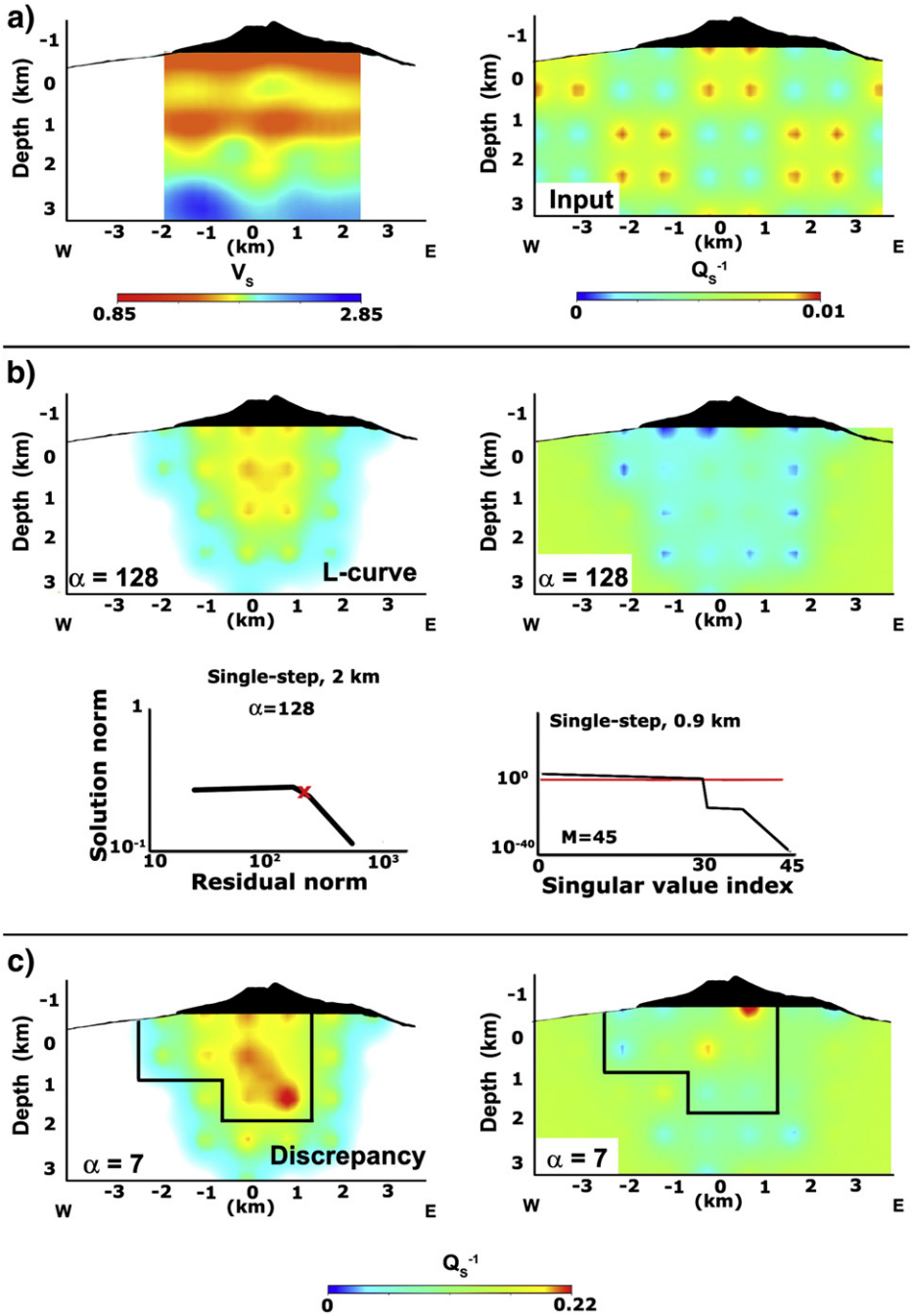

Fig. 8. a) Left-hand panel: the *S*-wave velocity under the volcanic edifice at MV on a cross-section through the 3-D velocity model of Scarpa et al. (2002). The input of the checkerboard test is shown on a vertical cross-section through the center of the volcanic edifice (right-hand panel). b) The left-hand tomogram shows a vertical slice through the single-step *S*-wave attenuation tomography results obtained by using the L-curve method. The corresponding output of the checkerboard test is shown in the right-hand tomogram. The smoothing parameter (α) is shown both in the lower left corner of each tomogram and as a red cross drawn on the L-curve. We also show the Picard condition related to this inversion. The red continuous lines represent the singular values. The black lines show the decrease in the dot product of the columns of the matrix spanning the data space and the data vector. c) Vertical slice through the single-step *S*-wave attenuation tomography results (left-hand panel), obtained by using the discrepancy principle, and the corresponding checkerboard test output (right-hand panel). The black line represents the regions described in the text, and defined following De Siena et al. (2009).

A small high attenuation anomaly has been found by De Siena et al. (2009) in the 18 Hz frequency band at around 1 km depth with a larger dataset and sources located at greater depths, and has been interpreted as a medium filled with fluids. The checkerboard tests provided in this last study in the area contoured by the black line (Fig. 8c) reproduce cubic anomalies of side 0.9 km. At this stage, considering the seismicity and the uncertainty of the average parameters, we cannot confirm that either the anomaly in Fig. 8b (L-curve) or Fig. 8c (Discrepancy) is the same as the one in De Siena et al. (2009), and any geological or volcanological interpretation would be meaningless.

The resolution tests show that the problem of our dataset is in the data, due either to the limits of the CN model or to the break of the ray approximation, not to the small number of rays crossing the cone region. De Siena et al. (2009) obtain stable and resolved results by

considering sources located outside of the region of maximum heterogeneity with a multi-step approach.

In our interpretation, these results confirm that adding waveforms produced by sources located in the regions of high heterogeneity and recorded at the cone without prior information coming from outside of these regions only decreases both stability and resolution. The diagonal elements of the resolution matrix, which are only dependent on the ray distribution, provide optimistic estimates of the attenuation tomography resolution below a volcanic cone (e.g., compare Fig. 7a,b).

3.5. Spatial and frequency limits of the tomographic imaging: aim of the multi-step structure

In both regions anomalous dependence of the energy ratios on the travel-time characterizes the data produced inside or just beneath the volcanic edifice at 3 Hz and 6 Hz. By merely using the corresponding seismicity located inside and/or beneath the volcanic edifice we obtain negative non-physical quality factors. We infer that these effects are induced in both cases by the increased reflectivity of the cone and/or by the higher heterogeneity of the velocity field inside the volcano. On the other hand, the frequency-dependent resonance of the seismic source energy in the volcanic feeding system could still be relevant at MSH (Chouet, 1988; Morozov, 2011; Margerin, 2013).

The CN method may not be applied at MV to data filtered at 3 Hz and 6 Hz at MV with the current seismicity (Fig. 5, see also De Siena et al. (2009)). The results at 18 Hz suggest instead that we require data that sample the cone laterally and/or at greater depths to provide reliable attenuation images of this volcano. In our interpretation, considering the present seismicity at MV, a direct measure of the transport mean free path by using the energy envelopes and the diffusion approximation is a better choice to model average *S*-wave attenuation inside and beneath the volcanic edifice at frequencies larger than 1 Hz (Wegler, 2003).

The attenuation images are still dependent on the velocity model, which is typically smoothing large velocity anomalies with a vertical velocity gradient. However, a gradual vertical velocity variation does not account for the strong variations suffered by the direct-wave energy in presence of highly heterogeneous structures. The strong scattering effects induced by a volcanic cone are considered a major source of loss of coherent direct-wave information. The existence of an infinite frequency ray associated with these energies in the typical frequency bands analyzed in volcano tomography (3 Hz, 6 Hz, 12 Hz, and 18 Hz) is questionable. The CN method, which requires a homogeneous scattering medium to measure total attenuation, is the best candidate to highlight these effects.

The inversion for the inverse Q provided by the CN method is perfectly linear in nature, as it is assumed that the velocity structure, the earthquake locations, and accordingly the ray paths are known. Thus, a solution can be attained for an arbitrary model parameterization in a single step, however, the multi-step scheme is designed to test and possibly the resolution in the area of maximum source sampling and interest. This provides information on the effect of the change in the scattering properties in the final model. The method accounts for regions of heterogeneous scattering, where the velocity structure may drastically change the behavior of the energy ratios with travel time. These regions are typically the ones of maximum earthquake nucleation inside and under the cone, and where negative average quality factors are obtained at a low frequency.

In order to compute and compare model uncertainties for the single-step and double-step Tikhonov inversions we should compute the error bounds of the regularization. These bounds would incorporate both sensitivity to noise and biases introduced by the Tikhonov regularization (chapter 5.8, Aster et al., 2005). However, it is meaningless to apply error bounds to a "true" model which is not smooth in any direction (attenuation, contrary to velocity, is not characterized by a vertical gradient). The differences between the regularized solution and the true model may actually be much larger than the confidence intervals, depending on the covariance matrix. In our opinion, the stability and checkerboard tests and their comparison with the resolution matrices performed for MSH are currently the only feasible approach to test tomographic images in the presence of a volcanic cone.

We do not aim to provide detailed attenuation tomography images of either of the two volcanoes, or an interpretation of them in terms of geological parameters. The main benefit of the MuRAT code is its ability to discriminate data affected by complex anomalous medium-dependent scattering. These phenomena produce frequency-dependent effects which are not adequately smoothed by a single linear inversion. With the multi-step algorithm we try to enlarge the range of frequencies that can be analyzed by confining these anomalous effects to the regions where they are actually observed. Hence, we add data that originated in different regions, but we do not let the attenuation parameters change in these other regions in the second inversion.

As for any method based on the "surgery of the feasible parameter models" (see, e.g., Van Wijk et al. (2002)) as well as on the use of deterministic prior information we change the range of data fitting given parameter models. A clear physical justification for this surgery is necessary in order to provide reliable limits for the regions showing systematic model errors. If these errors may be accounted for by a more efficient model, taking into account the effects of the increased heterogeneity, a single-step solution with an increased dataset sampling these regions only is preferable.

Comparing the tomographic images obtained for Mount St. Helens and Mount Vesuvius volcanoes striking correlations can be easily found, and misinterpreted in geological and geochemical terms. Our code is designed to help understand whether we can apply attenuation tomography to a volcanic area with a dataset previously used, e.g., for the velocity tomography. Nevertheless, the method mixes direct- and coda-wave information, that can produce models that are subject to over-interpretation if the assumptions of adequate source sampling and coda homogeneity are not fulfilled.

4. Conclusions

In volcano tomography, direct- and coda-wave energies are affected by strong frequency-dependent noise, which limits the range of frequencies that can be analyzed. This noise may be induced either by an uncertain source model or by complex medium-dependent effects. In both cases, the result is the anomalous increase of the direct-to-coda energy ratios with direct-wave travel time, which is caused both by the variations in coda energies recorded for different source-station geometries and by a spatially heterogeneous loss of direct-wave coherent information.

The MuRAT code provides tools to discriminate these frequency-dependent effects, to relate them to the regions of highest heterogeneity by using as data the seismic traces previously employed to obtain the velocity tomography results, and to understand their effects on attenuation tomography results. The aim of the code is both to obtain reliable attenuation tomograms and to put a constraint on the maximum resolution achievable in a larger range of frequencies than the one where attenuation tomography currently works. Tomographic images in different frequency bands are crucial to provide information on the scale of the deep volcanic structures.

The results in the two volcanic regions suggest that attenuation tomography can provide useful attenuation images between 3 Hz and 18 Hz at Mount St. Helens volcano if we increase the number of data by using volcano-tectonic earthquakes located at greater depths, just under the cone, and along the surrounding faults in different time periods. In our interpretation, the high attenuation affecting the cone in the single-step images is due to the effect of the cone, which increases scattering and focuses attenuation inside its structure. Due to the clustered seismicity at Mount Vesuvius, the method may instead be applied for the 18 Hz frequency band only. We can possibly enlarge the

frequency range if a different spatial distribution of seismic sources is made available, e.g., by using active seismicity.

Complete waveform information should ultimately be exploited with the aim to understand the complex interactions of a seismic wave-field in highly heterogeneous regions. The coda-normalization method, which allows for the inversion for the attenuation parameters from single-station recordings, with no need of source or site modeling, is a quick way to start achieving this goal. Its results provide a strong limitation to the actual resolution achievable under a volcanic cone, which we should overcome by a better and more complete theoretical understanding of the physical phenomena that both the source and the medium produce on the seismic wave-field.

Acknowledgments

The first author is grateful to Edoardo Del Pezzo and Francesca Bianco for the improvement upon the code during its testing and the large support given by them in the early stage of his career. We also thank Greg Waite for providing the *P*-wave velocity model of Mount St. Helens volcano. The facilities of the IRIS Data Management System, and specifically the IRIS Data Management Center, were used for access to waveform and metadata required in this study, and provided by the Cascades Volcano Observatory – USGS. We also thank the technicians and researchers working on the permanent and mobile stations at the Vesuvius Observatory – Istituto Nazionale di Geofisica e Vulcanologia. We finally thank the editor, Prof. Neuberg, and two anonymous reviewers for their insightful comments, that improved the quality of the paper. The MuRAT code with the two applications described above is freely available at http://earth.uni-muenster.de/~1desi_01/publications/publications.html under free license. The inversion procedures are mainly based on the codes developed by Hansen (1994).

References

Aki, K., 1980. Attenuation of shear-waves in the lithosphere for frequencies from 0.05 to 25 Hz. Phys. Earth Planet. Inter. 21, 50–60.
Aki, K., Richards, P., 1980. Quantitative Seismology — Theory and Methods. W. H. Freeman, San Francisco.
Aster, R., Borchers, B., Thurber, C., 2005. Parameter estimation and inverse problem. International Geophysics Series, Advances in Geophysics, vol. 90. Elsevier, Amsterdam.
Bai, C., Greenhalgh, S., 2005. 3D multi-step travel time tomography: imaging the local, deep velocity structure of Rabaul volcano, Papua New Guinea. Phys. Earth Planet. Inter. 151, 259–275.
Benz, H., Chouet, B.A., Dawson, P.B., Lahr, J.C., Page, R.A., Hole, J.A., 1996. Three-dimensional P and S wave velocity structure of Redoubt Volcano, Alaska. J. Geophys. Res. 101, 8111–8128.
Bianco, F., Castellano, M., Milano, G., Vilardo, G., Ferrucci, F., Gresta, S., 1999. The seismic crises at Mt. Vesuvius during 1995 and 1996. Phys. Chem. Earth 24, 977–983.
Block, L.V., 1991. Joint hypocenter–velocity inversion of local earthquake arrival time data in two geothermal regions. (Ph.D. dissertation) Massachusetts Institute of Technology, Cambridge.
Calvet, M., Margerin, L., 2013. Lapse time dependence of coda Q: anisotropic multiple-scattering models and application to Pyrenees. Bull. Seismol. Soc. Am. 103 (3), 1993–2010. http://dx.doi.org/10.1785/0120120239.
Cerveny, V., 2005. Seismic Ray Theory. Cambridge University Press.
Chouet, B., 1988. Resonance of a fluid-driven crack: radiation properties and implications for the source of long-period events and harmonic tremor. J. Geophys. Res. Solid Earth 93 (B5), 4375–4400 (1978–2012).
Chouet, B., 2003. Volcano seismology. PAGEOPH 160, 739–788.
Dahlen, F.A., Baig, A.M., 2002. Frechet kernels for body-wave amplitudes. Geophys. J. Int. 150, 440–466.
De Lorenzo, S., Gasparini, P., Mongelli, F., Zollo, A., 2001. Thermal state of the Campi Flegrei Caldera inferred from seismic attenuation tomography. J. Geodyn. 32, 476–486.
De Siena, L., Del Pezzo, E., Bianco, F., Tramelli, A., 2009. Multiple resolution seismic attenuation imaging at Mt. Vesuvius. Phys. Earth Planet. Inter. 173, 17–32.
De Siena, L., Del Pezzo, E., Bianco, F., 2010. Campi Flegrei seismic attenuation image: evidences of gas reservoirs, hydrothermal basins and feeding systems. J. Geophys. Res. 115 (B0), 9312–9329.
De Siena, L., Del Pezzo, E., Thomas, C., Curtis, A., Margerin, L., 2013. Seismic energy envelopes in volcanic media: in need of boundary conditions. Geophys. J. Int. 192 (1), 326–345.
Del Pezzo, E., Bianco, F., De Siena, L., Zollo, A., 2006. Small scale shallow attenuation structure at Mt. Vesuvius. Phys. Earth Planet. Inter. 157, 257–268.
Eberhart-Phillips, D., 1990. Three-dimensional P and S velocity structure in the Coalinga region, California. J. Geophys. Res. 95, 15343–15363.
Eberhart-Phillips, D., Chadwick, M., Bannister, S., 2008. Three-dimensional attenuation structure of central and southern south island, New Zealand, from local earthquakes. J. Geophys. Res. 113 (B05308). http://dx.doi.org/10.1029/2007JB005359.
Haberland, C., Rietbrock, A., 2001. Attenuation tomography in the western central Andes: a detailed insight into the structure of a magmatic arc. J. Geophys. Res. 106 (B6), 11151–11167.
Hansen, P.C., 1994. Regularization tools: a Matlab package for analysis and solution of discrete ill-posed problems. Numer. Algorithms 6 (1), 1–35.
Kissling, E., Ellsworth, W.L., Phillips, D.E., Kradolfer, U., 1994. Initial reference model in local earthquake tomography. J. Geophys. Res. 99 (B10), 19635–19646.
Koulakov, I., 2009. LOTOS code for local earthquake tomographic inversion, benchmarks for testing tomographic algorithms. Bull. Seismol. Soc. Am. 99, 194–214.
Koulakov, I., 2013. Studying deep sources of volcanism using multiscale seismic tomography. J. Volcanol. Geotherm. Res. 257, 205–226.
Koulakov, I., Bindi, D., Parolai, S., Grosser, H., Milkereit, C., 2010. Distribution of seismic velocities and attenuation in the crust beneath the North Anatolian Fault (Turkey) from local earthquake tomography. Bull. Seismol. Soc. Am. 100 (1), 207–224.
Lay, T., Wallace, T.C., 1995. Modern Global Seismology. Academic Press.
Lees, J., 1992. The magma system of Mount St. Helens: non-linear high-resolution P-wave tomography. J. Volcanol. Geotherm. Res. 53 (1), 103–116.
Lees, J.M., 2007. Seismic tomography of magmatic systems. J. Volcanol. Geotherm. Res. 167 (1), 37–56.
Lees, J.M., Lindley, G.T., 1994. Three-dimensional attenuation tomography at Loma Prieta: inverting t^* for Q. J. Geophys. Res. 99 (B4), 6843–6863.
MacCarthy, J.K., Borchers, B., Aster, R.C., 2011. Efficient stochastic estimation of the model resolution matrix diagonal and generalized cross-validation for large geophysical inverse problems. J. Geophys. Res. Solid Earth 116 (B10) (1978–2012).
Margerin, L., 2013. Diffusion approximation with polarization and resonance effects for the modelling of seismic waves in strongly scattering small-scale media. Geophys. J. Int. 192 (1), 326–345.
Marianelli, P., Metrich, N., Sbrana, A., 1999. Shallow and deep reservoirs involved in magma supply of the 1944 eruption of Vesuvius. Bull. Volcanol. 61, 48–63.
Matsumoto, S., Uehira, K., Watanabe, A., Goto, K., Iio, Y., Hirata, N., Okada, T., Takahashi, H., Shimizu, H., Shinohara, M., Kanazawa, T., 2009. High resolution Q-1 estimation based on extension of coda normalization method and its application to p-wave attenuation structure in the aftershock area of the 2005 west off Fukuoka prefecture earthquake (m 7.0). Geophys. J. Int. 179, 1039–1054.
Moran, S.C., Lees, J.M., Malone, S., 1999. P-wave crustal velocity structure in the greater Mount Rainier area from local earthquake tomography. J. Geophys. Res. 104 (B5), 10775–10786.
Morozov, I.B., 2008. Geometrical attenuation, frequency dependence of Q, and the absorption band problem. Geophys. J. Int. 175 (1), 239–252.
Morozov, I.B., 2011. Mechanisms of geometrical seismic attenuation. Ann. Geophys. 54 (3).
Neuberg, J., Pointer, T., 2000. Effects of volcano topography on seismic broad-band waveforms. Geophys. J. Int. 143, 239–248. http://dx.doi.org/10.1046/j.1365-246x.2000.00251.xs.
Nolet, G., 2008. A Breviary of Seismic Tomography, Imaging the Interior of the Earth and Sun. Cambridge University Press, New York.
Parsieglia, N., Wegler, U., 2008. Modelling of seismic energy transport at volcanoes with real topography and complex propagation medium. J. Volcanol. Geotherm. Res. 171, 229–236.
Quan, Y., Harris, J.M., 1996. Seismic tomography using the frequency shift method. Geophysics 62, 895–905.
Sato, H., Fehler, M.C., Maeda, T., 2012. Seismic Wave Propagation and Scattering in the Heterogeneous Earth, Second edition. Springer, New York, USA.
Scarpa, R., Tronca, F., Bianco, F., Del Pezzo, E., 2002. High resolution velocity structure beneath Mount Vesuvius from seismic array data. Geophys. Res. Lett. 21 (29), 2040.
Schurr, B., Asch, G., Rietbrock, A., Trumbull, R., Haberland, C.H., 2003. Complex patterns of fluid and melt transport in the central Andean subduction zone revealed by attenuation tomography. Earth Planet. Sci. Lett. 215, 105–119.
Sherrod, D.R., Scott, W.E., Stauffer, P.H. (Eds.), 2008. A Volcano Rekindled: The Renewed Eruption of Mount St. Helens, 2004–2006. US Geological Survey professional paper. US Geological Survey.
Thurber, C.H., 1987. Seismic structure and tectonics of Kilauea volcano Hawaii. In: Decker, R., Wright, T., Stauffer, P.H. (Eds.), Volcanism in Hawaii. US Geological Survey, USA, pp. 919–934.
Thurber, C.H., 1992. Hypocenter-velocity structure coupling in local earthquake tomography. Phys. Earth Planet. Inter. 75 (1), 55–62.
Thurber, C.H., Eberhart-Phillips, D., 1999. Local earthquake tomography with flexible gridding. Comput. Geosci. 25, 809–818.
Tusa, G., Malone, S.D., Giampiccolo, E., Gresta, S., Musumeci, C., 2004. Attenuation of short-period P waves at Mount St. Helens. Bull. Seismol. Soc. Am. 94 (4), 1441–1455. http://dx.doi.org/10.1785/012003040.
Van Wijk, K., Scales, J.A., Navidi, W., Tenorio, L., 2002. Data and model uncertainty estimation for linear inversion. Geophys. J. Int. 149 (3), 625–632.
Waite, G., Moran, S., 2009. Vp structure of Mount St. Helens, Washington, USA, imaged with local earthquake tomography. J. Volcanol. Geotherm. Res. 182, 113–122.
Waite, G., Chouet, B.A., Dawson, P.B., 2008. Eruption dynamics at Mount St. Helens imaged from broadband seismic waveforms: interaction of the shallow magmatic and hydrothermal systems. J. Geophys. Res. 113 (B2), B02305.

Wegler, U., 2003. Analysis of multiple scattering at Vesuvius Volcano, Italy, using data of the TomoVes active seismic experiment. J. Volcanol. Geotherm. Res. 128, 45–63.
Wegler, U., Lühr, B.G., 2001. Scattering behaviour at Merapi Volcano (Java) revealed from an active seismic experiment. Geophys. J. Int. 145, 579–592.
Xie, J., 2010. Can we improve estimates of seismological Q using a new geometrical spreading model? Pure Appl. Geophys. 167 (10), 1147–1162.
Yamamoto, M., Sato, H., 2010. Multiple scattering and mode conversion revealed by an active seismic experiment at Asama volcano, Japan. J. Geophys. Res. 115 (B0), 7304–7317.
Yoshimoto, K., Sato, H., Ohtake, M., 1993. Frequency-dependent attenuation of P and S waves in the Kanto Area, Japan, based on the coda-normalization method. Geophys. J. Int. 114, 165–174.